ELSEVIER

Engineering Analysis with Boundary Elements 29 (2005) 610–623

ENGINEERING ANALYSIS *with* BOUNDARY ELEMENTS

www.elsevier.com/locate/enganabound

A 2D time-domain BEM for transient wave scattering analysis by a crack in anisotropic solids

A. Tan[a], S. Hirose[b], Ch. Zhang[c,*], C.-Y. Wang[d]

[a]*Department of Civil Engineering, Tokyo Institute of Technology, Tokyo 152-8552, Japan*
[b]*Department of Mechanical and Environmental Informatics, Tokyo Institute of Technology, Tokyo 152-8552, Japan*
[c]*Department of Civil Engineering, University of Siegen, D-57068 Siegen, Germany*
[d]*Mathematics and Modeling Department, Schlumberger-Doll Research, Ridgefield, CT 06877-4108, USA*

Received 12 November 2004; revised 17 January 2005; accepted 18 January 2005
Available online 21 April 2005

Abstract

A two-dimensional (2D) time-domain boundary element method (BEM) is presented in this paper for transient analysis of elastic wave scattering by a crack in homogeneous, anisotropic and linearly elastic solids. A traction boundary integral equation formulation is applied to solve the arising initial-boundary value problem. A numerical solution procedure is developed to solve the time-domain boundary integral equations. A collocation method is used for the temporal discretization, while a Galerkin-method is adopted for the spatial discretization of the boundary integral equations. Since the hypersingular boundary integral equations are first regularized to weakly singular ones, no special integration technique is needed in the present method. Special attention of the analysis is devoted to the computation of the scattered wave fields. Numerical examples are given to show the accuracy and the reliability of the present time-domain BEM. The effects of the material anisotropy on the transient wave scattering characteristics are investigated.

Keywords: Time-domain boundary integral equation method; Galerkin-method; Transient elastic wave scattering; Crack analysis; Anisotropic solids

1. Introduction

The presence of cracks may dramatically change the mechanical behavior of the material and thus cause significant effects on the response and the integrity of a structure [50]. Ultrasonic techniques based on elastic wave propagation in solids are often utilized for quantitative nondestructive testing. The study of elastic wave scattering by cracks or crack-like defects could lead to a better evaluation of materials. Since scattered elastic waves can provide essential features for defect characterization, the simulation of the interaction between cracks and elastic waves is a key issue for developing efficient ultrasonic techniques for the evaluation and testing of elastic materials with cracks. From the wave scattering characteristics, the size, the location and the orientation of a crack can be determined.

Among many techniques available for the numerical simulation of elastic wave propagation in elastic solids, the boundary integral equation method (BIEM) or the boundary element method (BEM) provides an efficient and accurate numerical tool. In isotropic and linearly elastic solids, the BEM has already proved to be a capable method for modelling wave propagation phenomena [8–10,22,33]. Unfortunately, the conventional displacement BEM cannot be directly applied to solids involving cracks, since mathematically speaking a crack has two coincident points at the two opposite crack-faces. This degeneracy in the crack geometry leads to singular system matrices or degenerate BIE formulations [16]. Over the past years, many special procedures have been proposed to prevent the degeneration of the BEM formulation. Among them we just mention the crack Green's function method utilizing special Green's functions for a cracked solid [16,42], the sub-structuring or multi-domain method using the conventional

* Corresponding author. Tel.: +49 271 7402173; fax: +49 271 7402552.
E-mail address: c.zhang@uni-siegen.de (C. Zhang).

0955-7997/$ - see front matter © 2005 Elsevier Ltd. All rights reserved.
doi:10.1016/j.enganabound.2005.01.012

displacement BEM [8,22], the dual BEM by applying the displacement BIEs on one side of the crack-faces and the traction BIEs on the opposite side [5,6,15,23,24,31,38,43], and the traction BEM [10,16,25,26,35,51,55], where only one side of the crack-faces needs to be discretized.

Another complication in the transient BEM analysis arises for anisotropic and linearly elastic materials. This is due to the fact that the corresponding elastodynamic fundamental solutions or Green's functions for general anisotropic solids are mathematically very complicated and they cannot be expressed in explicit and simple forms. This unavoidable drawback of the time-domain Green's functions prohibits their easy numerical implementation and may affect the efficiency of the time-domain BEM/BIEM. For this reason, applications of the time-domain BEM to transient dynamic crack analysis are yet still very limited, though the BEM for elastostatic crack problems in anisotropic solids has been successfully developed and applied by using different formulations (e.g. [5,17,18,20,21, 25,32,36,37]).

Different BEM formulations can be found in literature for transient crack analysis in anisotropic materials. To avoid the use of the complex fundamental solutions for anisotropic materials, the dual reciprocity BEM has been proposed, where the corresponding elastostatic fundamental solutions are applied [2–4,23,24]. This method requires certain interior nodes to accurately describe the initial effects. A time-domain displacement BEM for transient wave scattering analysis by cavities has been developed by Wang et al. [48]. The method used the time-domain elastodynamic fundamental solutions for anisotropic solids, which have been derived by Wang and Achenbach [47] by using Radon-transform. Later, the time-domain displacement BEM has been extended to transient crack analysis in anisotropic solids, where the traction BIEs have been applied [28–30]. By using the same set of traction BIEs, Zhang presented an alternative time-stepping scheme by using a convolution quadrature formula and the Laplace-transformed fundamental solutions [52–54]. A comparative study of both time-domain BEM has been performed by Hirose et al. [30]. Applications of hypersingular traction BIEs to time-harmonic and transient dynamic crack analysis have also been presented in [7,11–13,26,39,40]. A literature review on the subject can be found in [14,52].

In this paper, we present a two-dimensional (2D) time-domain traction BEM for transient wave scattering analysis by a crack in homogeneous, linearly elastic and general anisotropic solids. A finite crack contained in an infinite, homogeneous, linearly elastic and anisotropic solid subjected to transient incident wave loading is investigated. Two-dimensional generalized plane-strain or plane-stress condition is considered. The initial-boundary value problem is formulated as a set of hypersingular time-domain traction BIEs with the crack-opening-displacements (CODs) as the unknown quantities. The hypersingular integrals are regarded as Hadamard finite-part integrals. A time-stepping scheme is developed for solving the time-domain traction BIEs. The time-domain elastodynamic fundamental solutions derived by Wang and Achenbach [47] have been used. The time-convolution is approximated by a collocation method, while the spatial discretization of the time-domain BIEs is performed by using a spatial Galerkin-method. Integrations with respect to spatial and time variables are carried out analytically, and only the integration over the unit circle arising in the dynamic part of the fundamental solutions is done numerically. After the CODs have been obtained numerically, the scattered displacement wave field can be computed by using the integral representation formula for the scattered displacements. Numerical results are presented and discussed. For isotropic solids, the time variations of the CODs are compared to that obtained by the conventional time-domain BEM with the isotropic fundamental solutions. To check the reliability of the present time-domain traction BEM, a flat elliptical cavity with a very small minor to major axis ratio is also investigated, where the time-domain displacement BEM has been used. The scattered wave fields for a crack and a cavity with the same length show strikingly similar patterns, which confirms the reliability of the present time-domain traction BEM. The effects of the material anisotropy on the transient wave scattering characteristics are analyzed via numerical examples.

2. Problem statement

We consider a two-dimensional (2D), infinite, linearly elastic and anisotropic solid containing a finite crack of arbitrary shape as depicted in Fig. 1. Rectangular Cartesian coordinate system is used. In the absence of body forces, the solid satisfies the equations of motion [1]

$$\sigma_{i\beta,\beta} = \rho \ddot{u}_i, \tag{1}$$

and the Hooke's law

$$\sigma_{i\beta} = C_{i\beta k\lambda} u_{k,\lambda}, \tag{2}$$

where u_i and $\sigma_{i\beta}$ are the displacement and the stress components, ρ is the mass density and $C_{i\beta k\lambda}$ is

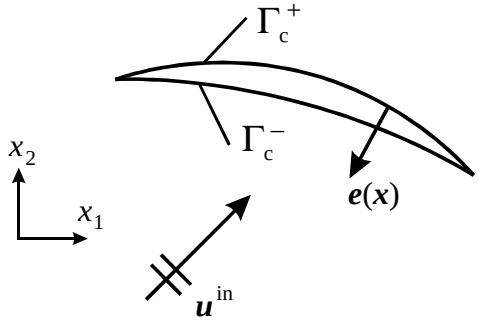

Fig. 1. Wave scattering by a crack.

the fourth-order elasticity tensor, respectively. A comma after a quantity denotes partial derivative with respect to spatial variables, and the conventional summation rule over repeated indices is applied throughout the paper. Also, Roman suffixes have values of 1, 2 and 3, while Greek suffixes take values of 1 and 2 only. Substitution of Eq. (2) into Eq. (1) yields the following equations of motion for the displacement components

$$[\Gamma_{ij}(\partial_1,\partial_2)-\rho\delta_{ij}\partial_t^2]u_j(x,t)=0, \tag{3}$$

where

$$\Gamma_{ij}(\partial_1,\partial_2)=C_{i\alpha j\beta}\partial_\alpha\partial_\beta, \tag{4}$$

is the second-order Christoffel tensor, and ∂_α represents partial derivative with respect to a spatial variable x_α. Note here that though the displacement and the stress fields in the 2D analysis are independent of the x_3-coordinate, the in-plane and the anti-plane deformations are generally not decoupled in anisotropic solids.

An incident elastic wave interacts with the crack which induces scattered waves. Thus, the total wave field can be written as

$$u_i=u_i^{\mathrm{in}}+u_i^{\mathrm{sc}},\quad t_i=t_i^{\mathrm{in}}+t_i^{\mathrm{sc}}, \tag{5}$$

where $t_i=\sigma_{i\beta}e_\beta$ represents the traction vector with e_β being the outward unit normal vector to the crack-faces. Also, the superscript 'in' denotes the incident wave field, while 'sc' stands for the scattered wave field.

As initial conditions, we assume

$$u_i(\mathbf{x},t)=\dot{u}_i(\mathbf{x},t)=0,\quad t=0. \tag{6}$$

On the crack-faces, traction-free boundary conditions are assumed, i.e.

$$t_i(\mathbf{x},t)=\sigma_{i\beta}(\mathbf{x},t)e_\beta(\mathbf{x})=0,\quad \mathbf{x}\in\Gamma_{\mathrm{c}}, \tag{7}$$

where $\Gamma_{\mathrm{c}}=\Gamma_{\mathrm{c}}^+ + \Gamma_{\mathrm{c}}^-$ denotes the crack-faces with Γ_{c}^+ and Γ_{c}^- being the upper and the lower one.

The incident wave fields are given, while the scattered wave fields have to be determined by using the partial differential equation (3) in conjunction with the initial and the boundary conditions (6) and (7). This can be done by using a time-domain boundary integral equation formulation as will be shown in Section 3.

3. Time-domain boundary integral equations

By using the Betti–Rayleigh reciprocal theorem, a representation integral for the displacement components can be obtained as [1]

$$u_k(\mathbf{y},t)=u_k^{\mathrm{in}}(\mathbf{y},t)-\int_{\Gamma_{\mathrm{c}}^+}h_{ik}(\mathbf{x},\mathbf{y};t)*\Delta u_i(\mathbf{x},t)\mathrm{d}s_x,\quad \mathbf{y}\notin\Gamma_{\mathrm{c}}^+, \tag{8}$$

where $\mathbf{x}$ and $\mathbf{y}$ are the source and the observation points, $h_{ik}(\mathbf{x},\mathbf{y};t)$ is the time-domain elastodynamic traction fundamental solution defined by

$$h_{ik}(\mathbf{x},\mathbf{y};t)=C_{i\alpha j\beta}e_\alpha(\mathbf{x})g_{jk,\beta}(\mathbf{x},\mathbf{y};t) \tag{9}$$

with $g_{jk}(\mathbf{x},\mathbf{y};t)$ being the time-domain displacement fundamental solution, and an * stands for Riemann convolution

$$g(\mathbf{x},t)*h(\mathbf{x},t)=\int_0^t g(\mathbf{x},t-\tau)h(\mathbf{x},\tau)\mathrm{d}\tau. \tag{10}$$

In Eq. (8), $\Delta u_i(\mathbf{x},t)$ are the crack-opening-displacements (CODs) defined by

$$\Delta u_i(\mathbf{x},t)=u_i(\mathbf{x}\in\Gamma_{\mathrm{c}}^+,t)-u_i(\mathbf{x}\in\Gamma_{\mathrm{c}}^-,t). \tag{11}$$

A direct limit process $\mathbf{y}\to\Gamma_{\mathrm{c}}^+$ in Eq. (8) leads to a degenerate boundary integral equation formulation [16]

$$\frac{1}{2}[u_k(\mathbf{y}\in\Gamma_{\mathrm{c}}^+,t)+u_k(\mathbf{y}\in\Gamma_{\mathrm{c}}^-,t)]=u_k^{\mathrm{in}}(\mathbf{y},t)-\mathrm{p.v.}\int_{\Gamma_{\mathrm{c}}^+}h_{ik}(\mathbf{x},\mathbf{y};t)*\Delta u_i(\mathbf{x},t)\mathrm{d}s_x,\quad \mathbf{y}\in\Gamma_{\mathrm{c}}^+, \tag{12}$$

where p.v. means the principal value integral. If Γ_{c}^+ is smooth, a natural way to overcome this difficulty is the use of the traction boundary integral equation formulation. For this purpose, we substitute Eq. (8) into Hooke's law (2) to obtain the following integral representation for the traction components

$$t_j(\mathbf{y},t)=t_j^{\mathrm{in}}(\mathbf{y},t)-\int_{\Gamma_{\mathrm{c}}^+}w_{ij}(\mathbf{x},\mathbf{y};t)*\Delta u_i(\mathbf{x},t)\mathrm{d}s_x,\quad \mathbf{y}\notin\Gamma_{\mathrm{c}}^+, \tag{13}$$

where $w_{ij}(\mathbf{x},\mathbf{y};t)$ is the higher-order traction fundamental solution which is defined by

$$w_{ij}(\mathbf{x},\mathbf{y};t)=C_{i\gamma p\delta}C_{j\alpha k\beta}e_\gamma(\mathbf{x})e_\alpha(\mathbf{y})\frac{\partial^2 g_{pk}(\mathbf{x},\mathbf{y};t)}{\partial \mathrm{x}_\delta\partial \mathrm{y}_\beta}. \tag{14}$$

By taking the limit process $\mathbf{y}\to\Gamma_{\mathrm{c}}^+$ and considering the traction boundary conditions (7), time-domain traction BIEs are obtained as

$$\mathrm{f.p.}\int_{\Gamma_{\mathrm{c}}^+}w_{ij}(\mathbf{x},\mathbf{y};t)*\Delta u_i(\mathbf{x},t)\mathrm{d}s_x=t_j^{\mathrm{in}}(\mathbf{y},t),\quad \mathbf{y}\in\Gamma_{\mathrm{c}}^+, \tag{15}$$

where f.p. denotes the Hadamard finite part integral. As will be shown in Section 4, the higher-order fundamental solution $w_{ij}(\mathbf{x},\mathbf{y};t)$ can be split into a singular static part $w_{ij}^{\mathrm{s}}(\mathbf{x},\mathbf{y})$ and a regular dynamic part $w_{ij}^{\mathrm{d}}(\mathbf{x},\mathbf{y};t)$ according to

$$w_{ij}(\mathbf{x},\mathbf{y};t)*f(t)=w_{ij}^{\mathrm{s}}(\mathbf{x},\mathbf{y})f(t)+w_{ij}^{\mathrm{d}}(\mathbf{x},\mathbf{y};t)*\ddot{f}(t). \tag{16}$$

By invoking Eq. (16), we can rewrite Eq. (15) as

$$\text{f.p.}\int_{\Gamma_c^+} w_{ij}^{s}(\mathbf{x},\mathbf{y})\Delta u_i(\mathbf{x},t)\mathrm{d}s_x + \int_{\Gamma_c^+} w_{ij}^{d}(\mathbf{x},\mathbf{y};t) * \Delta\ddot{u}_i(\mathbf{x},t)\mathrm{d}s_x = t_j^{in}(\mathbf{y},t), \quad \mathbf{y}\in\Gamma_c^+. \tag{17}$$

It should be noted here that the first term in the time-domain traction BIEs (17) has a hypersingularity and it should be understood in the sense of Hadamard finite-part integral. In contrast, the second integral in Eq. (17) is regular. Though several techniques are available to deal with the hypersingular integrals [41,45,50], a Galerkin-method is applied in this paper for the spatial discretization of the hypersingular time-domain BIEs. An essential advantage of the Galerkin-method presented in this paper is that the method does not require any special regularization or integration technique for computing the arising hypersingular integrals.

4. Time-domain dynamic fundamental solutions

The dynamic fundamental solutions or Green's functions are solutions of the following partial differential equations

$$[\Gamma_{ki}(\partial_1,\partial_2) - \rho\delta_{ki}\partial_t^2]g_{ij}(\mathbf{x},\mathbf{y};t) = -\delta_{kj}\delta(\mathbf{x}-\mathbf{y})\delta(t) \tag{18}$$

with the initial conditions

$$g_{ij}(\mathbf{x},\mathbf{y};t) = 0, \quad \text{for } t\le 0. \tag{19}$$

By applying the Radon transform to Eqs. (18) and (19), Wang and Achenbach obtained the following displacement fundamental solution [47]

$$g_{ij}(\mathbf{x},\mathbf{y};t) = \frac{H(t)}{4\pi^2}\int_{|\mathbf{n}|=1}\sum_{l=1}^{L}\frac{P_{ij}^l}{\rho c_l}\left(\frac{1}{c_l t+\mathbf{n}\cdot(\mathbf{x}-\mathbf{y})}\right)\mathrm{d}\mathbf{n}, \tag{20}$$

where $P_{ij}^l = E_{il}E_{jl}$ is the projection operator, while E_{ij} and c_l are the eigenvectors and the eigenvalues of the matrix

$$\Gamma_{ik}(n_1,n_2) = C_{i\alpha k\beta}n_\alpha n_\beta, \tag{21}$$

in which $\mathbf{n}$ denotes the wave propagation vector. By substituting Eq. (20) into Eq. (9), we obtain the time-domain traction fundamental solution as

$$h_{ij}(\mathbf{x},\mathbf{y};t) = \frac{H(t)}{4\pi^2}\int_{|\mathbf{n}|=1}\sum_{l=1}^{L}\frac{Q_{ij}^l}{\rho c_l^2}\frac{\partial}{\partial t}\left(\frac{1}{c_l t+\mathbf{n}\cdot(\mathbf{x}-\mathbf{y})}\right)\mathrm{d}\mathbf{n}, \tag{22}$$

in which

$$Q_{ij}^l = C_{i\alpha k\beta}e_\alpha(\mathbf{x})n_\beta P_{kj}^l(\mathbf{n}). \tag{23}$$

Higher-order time-domain traction fundamental solution can be obtained by substituting Eq. (20) into Eq. (14), which results in

$$w_{ij}(\mathbf{x},\mathbf{y};t) = -\frac{H(t)}{4\pi^2}\int_{|\mathbf{n}|=1}\sum_{l=1}^{L}\frac{R_{ij}^l}{\rho c_l^3}\frac{\partial^2}{\partial t^2}\left(\frac{1}{c_l t+\mathbf{n}\cdot(\mathbf{x}-\mathbf{y})}\right)\mathrm{d}\mathbf{n}, \tag{24}$$

where use is made of the derivative transfer of spatial variables to time variable t, and

$$R_{ij}^l = C_{i\gamma p\delta}C_{j\alpha k\beta}n_\delta n_\beta e_\gamma(\mathbf{x})e_\alpha(\mathbf{y})P_{pk}^l(\mathbf{n}). \tag{25}$$

Now we consider the following time convolution

$$w_{ij}(\mathbf{x},\mathbf{y};t) * f(t) = -\frac{1}{4\pi^2}\int_{|\mathbf{n}|=1}\sum_{l=1}^{L}\frac{R_{ij}^l}{\rho c_l^3}\left[\int_0^t\frac{\partial^2}{\partial\tau^2}\left(\frac{1}{c_l\tau+\mathbf{n}\cdot(\mathbf{x}-\mathbf{y})}\right)f(t-\tau)\mathrm{d}\tau\right]\mathrm{d}\mathbf{n}. \tag{26}$$

Integrating Eq. (26) by parts twice with respect to time t we obtain

$$\begin{aligned} w_{ij}(\mathbf{x},\mathbf{y};t) * f(t) &= -\frac{1}{4\pi^2}\int_{|\mathbf{n}|=1}\sum_{l=1}^{L}\frac{R_{ij}^l}{\rho c_l^3}\left[\frac{c_l}{(\mathbf{n}\cdot(\mathbf{x}-\mathbf{y}))^2}f(t) + \int_0^t\frac{1}{c_l\tau+\mathbf{n}\cdot(\mathbf{x}-\mathbf{y})}\ddot{f}(t-\tau)\mathrm{d}\tau\right]\mathrm{d}\mathbf{n} \\ &= w_{ij}^{s}(\mathbf{x},\mathbf{y})f(t) + w_{ij}^{d}(\mathbf{x},\mathbf{y};t) * \ddot{f}(t), \end{aligned} \tag{27}$$

where

$$w_{ij}^{s}(\mathbf{x},\mathbf{y}) = -\frac{1}{4\pi^2}\int_{|\mathbf{n}|=1}\sum_{l=1}^{L}\frac{R_{ij}^l}{\rho c_l^2}\frac{1}{(\mathbf{n}\cdot(\mathbf{x}-\mathbf{y}))^2}\mathrm{d}\mathbf{n}, \tag{28}$$

$$w_{ij}^{d}(\mathbf{x},\mathbf{y};t) = -\frac{H(t)}{4\pi^2}\int_{|\mathbf{n}|=1}\sum_{l=1}^{L}\frac{R_{ij}^l}{\rho c_l^3}\frac{1}{c_l t+\mathbf{n}\cdot(\mathbf{x}-\mathbf{y})}\mathrm{d}\mathbf{n}, \tag{29}$$

Eq. (27) implies that the elastodynamic fundamental solution can be split into a static part and a dynamic part. The static part corresponds to the elastostatic fundamental solution which is hypersingular. In contrast, the dynamic part is regular except at the wave front $c_l t+\mathbf{n}\cdot(\mathbf{x}-\mathbf{y})=0$. It should be noted here that by using the same idea the displacement and the traction fundamental solutions can also be split into their static and dynamic parts, but they are not given here for the sake of brevity.

The static fundamental solutions have closed-form solutions. For instance, the static displacement fundamental solution has the following explicit form [19,49]

$$g_{ij}^{s}(\mathbf{x},\mathbf{y}) = \frac{1}{\pi}\mathrm{Im}\sum_{l=1}^{L}\frac{A_{ij}(\eta_l)}{\partial_\eta D(\eta_l)}\log(z_l) + \alpha_{ij}, \tag{30}$$

where

$$A_{ij}(\eta) = \mathrm{adj}[\Gamma_{ij}(1,\eta)], \quad D(\eta) = \det[\Gamma_{ij}(1,\eta)], \tag{31}$$

$$z_l = x_1 - y_1 + \eta_l(x_2 - y_2), \quad l = 1,2,3, \tag{32}$$

$$\alpha_{ij} = -\frac{1}{4\pi^2} \int_{|\mathbf{n}|=1} \Gamma_{ij}^{-1}(\mathbf{n}) \log|n_1| \, \mathrm{d}n$$

$$= -\frac{1}{\pi} \mathrm{Im} \sum_{l=1}^{L} \frac{A_{ij}(\eta_l)}{\partial_\eta D(\eta_l)} \log(\eta_l + i), \tag{33}$$

In Eq. (30), η_l are distinct roots of the characteristic equation

$$D(\eta_l) = 0, \quad \mathrm{Im}(\eta_l) > 0, \quad l = 1,2,3. \tag{34}$$

Since $\Gamma_{ij}(1,\eta)$ is real, symmetric and positive definite, its determinant can never be zero unless η is complex. It is remarked here that the constant term α_{ij} in the static fundamental solution (30) is necessary to maintain the quiescent field ahead of the wave fronts generated by a point force. For static analysis, this term is inessential.

The higher-order static traction fundamental solution can also be reduced to a closed-form expression by applying the Stroh's formalism [44,46]. By substituting Eq. (30) into Eq. (14) and then applying the Stroh's formalism twice, we obtain [28]

$$w_{ij}^{\mathrm{s}}(\mathbf{x},\mathbf{y}) = \frac{1}{\pi} \frac{\partial}{\partial s_x} \frac{\partial}{\partial s_y} \mathrm{Im} \sum_{l=1}^{L} B_{ij}^{l}(\eta_l) \log[\mathbf{d}_l \cdot (\mathbf{x} - \mathbf{y})], \tag{35}$$

in which

$$B_{ij}^{l}(\eta_l) = \frac{(M_{ip} + L_{ip}\eta_l) A_{pk}(\eta_l) (M_{jk} + L_{jk}\eta_l)}{\partial D(\eta_l)}, \tag{36}$$

$\mathbf{d}_l = (1, \eta_l)$.

In Eq. (36), L_{ij} and M_{ij} are defined by the following equation

$$\Gamma_{ij}(1,\eta) = L_{ij}\eta^2 + (M_{ij} + M_{ij}^T)\eta + N_{ij}, \tag{37}$$

where

$$N_{ij} = C_{i1j1}, \quad M_{ij} = C_{i1j2}, \quad L_{ij} = C_{i2j2}. \tag{38}$$

Here, it should be noted again that the higher-order static traction fundamental solution has a hypersingularity at $\mathbf{x} = \mathbf{y}$ as can be seen from Eq. (35).

5. Numerical solution procedure

An efficient numerical solution procedure is developed to solve the hypersingular time-domain traction BIEs (17). A Galerkin-method is used for the spatial discretization, while a collocation method is applied for the temporal discretization of the time-domain BIEs. For this purpose, the unknown CODs Δu_i $(\mathbf{x},t)$ are approximated by the following interpolation functions

$$\Delta u_i(\mathbf{x},t) = \sum_{q=1}^{Q} \sum_{n=1}^{N} \phi_u^n(\mathbf{x}) \varphi_u^q(t) (\Delta u_i)^{nq}, \tag{39}$$

where n denotes the nth node, q represents the qth time-step, $\phi_u^n(\mathbf{x})$ and $\varphi_u^q(t)$ are the spatial and the temporal shape functions, respectively. Multiplying both sides of Eq. (17) by $\phi_u^m(\mathbf{y})$ and integrating them with respect to s_y we obtain

$$\int_{\Gamma_c^+} \phi_u^m(\mathbf{y}) \mathrm{d}s_y \int_{\Gamma_c^+} w_{ij}^{\mathrm{s}}(\mathbf{x},\mathbf{y}) \Delta u_i(\mathbf{x},t) \mathrm{d}s_x$$

$$+ \int_{\Gamma_c^+} \phi_u^m(\mathbf{y}) \mathrm{d}s_y \int_{\Gamma_c^+} w_{ij}^{\mathrm{d}}(\mathbf{x},\mathbf{y};t) * \Delta\ddot{u}_i(\mathbf{x},t) \mathrm{d}s_x$$

$$= \int_{\Gamma_c^+} \phi_u^m(\mathbf{y}) t_j^{\mathrm{in}}(\mathbf{y},t) \mathrm{d}s_y, \quad \mathbf{y} \in \Gamma_c^+. \tag{40}$$

Substitution of the explicit form of the higher-order traction fundamental solution (35) into Eq. (40) yields

$$\int_{\Gamma_c^+} \phi_u^m(y) \mathrm{d}s_y \int_{\Gamma_c^+} \frac{1}{\pi} \frac{\partial}{\partial s_x} \frac{\partial}{\partial s_y} \mathrm{Im} \sum_{l=1}^{L} B_{ij}^{l}(\eta_l) \log[\mathbf{d}_l \cdot (\mathbf{x} - \mathbf{y})]$$

$$\Delta u_i(\mathbf{x},t) \mathrm{d}s_x + \int_{\Gamma_c^+} \phi_u^m(\mathbf{y}) \mathrm{d}s_y \int_{\Gamma_c^+} w_{ij}^{d}(\mathbf{x},\mathbf{y};t) * \Delta\ddot{u}_i(\mathbf{x},t) \mathrm{d}s_x$$

$$= \int_{\Gamma_c^+} \phi_u^m(\mathbf{y}) t_j^{\mathrm{in}}(\mathbf{y},t) \mathrm{d}s_y, \quad \mathbf{y} \in \Gamma_c^+. \tag{41}$$

By using the technique of partial integration in conjunction with $\phi_u^m = 0$ and $\Delta u_i = 0$ at the crack-tips, we can transfer the spatial derivatives of the higher-order static traction fundamental solution to the spatial shape function and the CODs. This results in

$$\int_{\Gamma_c^+} \frac{\partial \phi_u^m(\mathbf{y})}{\partial s_y} \mathrm{d}s_y \int_{\Gamma_c^+} \frac{1}{\pi} \mathrm{Im} \sum_{l=1}^{L} B_{ij}^{l}(\eta_l) \log[\mathbf{d}_l \cdot (\mathbf{x} - \mathbf{y})]$$

$$\times \frac{\partial \Delta u_i(\mathbf{x},t)}{\partial s_x} \mathrm{d}s_x + \int_{\Gamma_c^+} \phi_u^m(\mathbf{y}) \mathrm{d}s_y \int_{\Gamma_c^+} w_{ij}^{d}(\mathbf{x},\mathbf{y};t) * \Delta\ddot{u}_i(\mathbf{x},t) \mathrm{d}s_x$$

$$= \int_{\Gamma_c^+} \phi_u^m(\mathbf{y}) t_j^{\mathrm{in}}(\mathbf{y},t) \mathrm{d}s_y, \quad \mathbf{y} \in \Gamma_c^+. \tag{42}$$

It should be remarked here that the Galerkin-BIEs (42) represent a regularized version of the hypersingular boundary integral equations (17), and they have only a weak singularity.

Using the following spatial and temporal discretizations

$$\Gamma_c^+ = \sum_{n=1}^{N} \Gamma_n, \quad t = Q\,\Delta t, \tag{43}$$

the BIEs (42) can be converted into a system of linear algebraic equations as follows

$$\sum_{n=1}^{N}\left(W_{ij}^{s;m,n}(\Delta u_i)^{nQ}+\sum_{q=1}^{Q}W_{ij}^{d;m,n,Q-q+1}(\Delta u_i)^{nq}\right)=\sum_{n=1}^{N}D^{mn}t_j^{\mathrm{in},nQ},\tag{44}$$

where the system matrices $W_{ij}^{s;m,n}$, $W_{ij}^{d;m,n,q}$ and D^{mn} are given by

$$W_{ij}^{s;m,n}=\frac{1}{\pi}\int_{\Gamma_m}\frac{\partial\phi_u^m(y)}{\partial s_y}\mathrm{d}s_y\int_{\Gamma_n}\frac{\partial\phi_u^n(x)}{\partial s_x}\times\mathrm{Im}\sum_{l=1}^{L}\{B_{ij}^l(\eta_l)\log[\mathbf{d}_l\cdot(\mathbf{x}-\mathbf{y})]\}\mathrm{d}s_x,\tag{45}$$

$$W_{ij}^{d;m,n,Q-q+1}=\frac{1}{\pi}\int_{\Gamma_m}\phi_u^m(\mathbf{y})\mathrm{d}s_y\int_{\Gamma_n}w_{ij}^d(\mathbf{x},\mathbf{y};Q\,\Delta t)*\ddot{\varphi}_u^q(Q\,\Delta t)\phi_u^n(\mathbf{x})\mathrm{d}s_x,\tag{46}$$

$$D^{mn}=\int_{\Gamma_m}\phi_u^m(y)\phi_t^n(y)\mathrm{d}s_y,\tag{47}$$

where $\phi_t^n(\mathbf{y})$ is the spatial shape function for the traction components.

In this analysis, we use linear shape functions for both the temporal and the spatial shape functions $\varphi_u^q(t)$, $\phi_u^n(\mathbf{x})$ and $\phi_t^n(\mathbf{y})$. The temporal shape function $\varphi_u^q(t)$ is shown in Fig. 2, which can be expressed as

$$\varphi_u^q(t)=\frac{1}{\Delta t}\{[t-(q-1)\Delta t]H[t-(q-1)\Delta t]-2(t-q\,\Delta t)\times H(t-q\,\Delta t)+[t-(q+1)\Delta t]H[t-(q+1)\Delta t]\},\tag{48}$$

in which $H(\cdot)$ is the Heaviside function. The time derivatives of the temporal shape function $\ddot{\varphi}_u^q(t)$ is then given by

$$\ddot{\varphi}_u^q(t)=\frac{1}{\Delta t}\{\delta[t-(q-1)\Delta t]-2\delta(t-q\,\Delta t)+\delta[t-(q+1)\Delta t]\}.\tag{49}$$

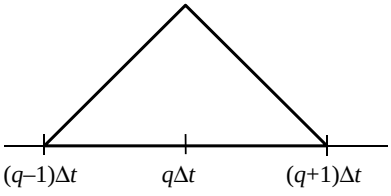

Fig. 2. Temporal shape function $\varphi_u^q(t)$.

With Eq. (49), the time convolution in Eq. (46) can be evaluated analytically as

$$w_{ij}^{\mathrm{d}}(\mathbf{x},\mathbf{y};Q\,\Delta t)*\ddot{\varphi}_u^q(Q\,\Delta t)=\frac{1}{\Delta t}\{w_{ij}^{\mathrm{d}}[\mathbf{x},\mathbf{y};(Q-(q-1))\Delta t)]-2w_{ij}^{\mathrm{d}}[\mathbf{x},\mathbf{y};(Q-q)\Delta t]+w_{ij}^{\mathrm{d}}[\mathbf{x},\mathbf{y};(Q-(q+1))\Delta t]\}.\tag{50}$$

Since a linear spatial shape function is chosen, the spatial integrations arising in the system matrices can also be computed analytically. The final results are given in Appendix A. Only the dynamic part of the system matrix containing the integral over a unit circle has to be computed numerically. This special feature makes the present time-domain BEM especially attractive. The discrete CODs can be computed numerically from Eq. (44) time-step by time-step.

Once the CODs have been obtained numerically, the scattered displacement field can be computed by using the integral representation formula [48]

$$u_j^{\mathrm{sc}}(\mathbf{y},t)=-\int_{\Gamma_{\mathrm{c}}^+}h_{ij}(\mathbf{x},\mathbf{y};t)*\Delta u_i(\mathbf{x},t)\mathrm{d}s_x.\tag{51}$$

By using the static and the dynamic parts of the traction fundamental solution we obtain the following equation for computing the scattered displacement field at the time-step $Q\,\Delta t$

$$u_j^{\mathrm{sc},Q}(\mathbf{y})=-\sum_{n=1}^{N}\left[H_{ij}^{\mathrm{s};n}(\mathbf{y})\Delta u_i^{nQ}+\sum_{q=1}^{Q}H_{ij}^{\mathrm{d};n,Q-q+1}(\mathbf{y})\Delta u_i^{nq}\right],\tag{52}$$

where the matrices $H_{ij}^{\mathrm{s};n}(\mathbf{y})$ and $H_{ij}^{\mathrm{d};n,Q-q+1}(\mathbf{y})$ are given by

$$H_{ij}^{\mathrm{s};n}(\mathbf{y})=\int_{\Gamma_n}h_{ij}^{\mathrm{s}}(\mathbf{x},\mathbf{y})\phi_u^n(\mathbf{x})\,\mathrm{d}s_x,\tag{53}$$

$$H_{ij}^{\mathrm{d};n,Q-q+1}(\mathbf{y})=\int_{\Gamma_n}h_{ij}^{\mathrm{d}}(\mathbf{x},\mathbf{y};Q\,\Delta t)*\ddot{\varphi}_u^q(Q\,\Delta t)\phi_u^n(\mathbf{x})\mathrm{d}s_x.\tag{54}$$

It should be remarked here that the CODs have a local square-root behavior near the crack-tips. For this reason, we

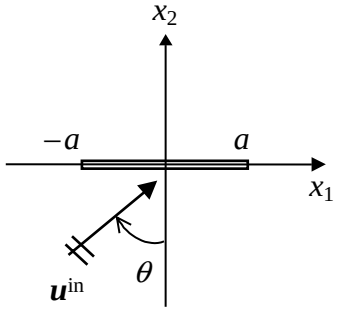

Fig. 3. A finite crack of length $2a$.

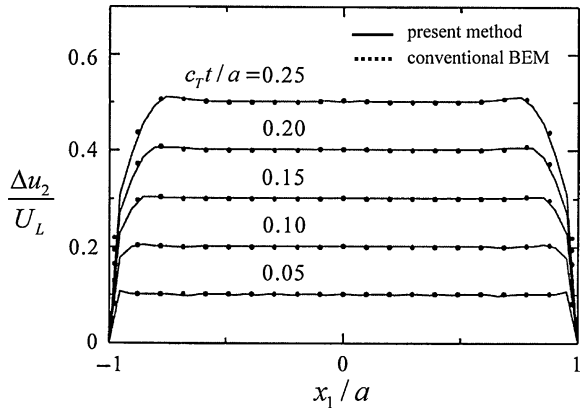

Fig. 4. Time variations of $\Delta u_2/U_L$ for a crack and a normal incidence of a plane L-wave in an isotropic solid.

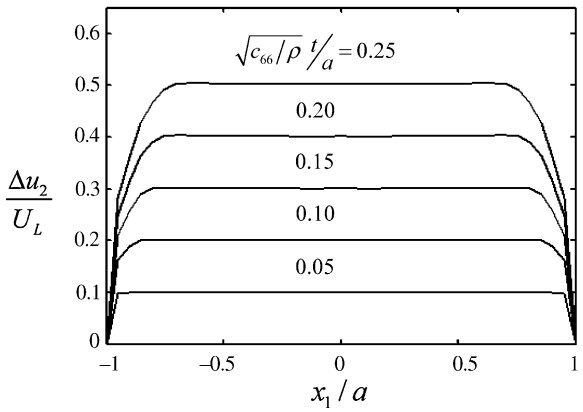

Fig. 6. Time variations of $\Delta u_2/U_L$ for a crack and a normal incidence of a quasi L-wave in a transversely isotropic solid.

also adopted crack-tip elements near the crack-tips to approximate the local behavior of the CODs correctly. However, our extensive numerical tests have shown that the use of crack-tip elements does not give a notable improvement as long as the scattered displacements are concerned.

6. Numerical examples

To check the accuracy and the efficiency of the present time-domain BEM, we first consider a finite crack of length $2a$ in an infinite, linearly elastic and isotropic solid as depicted in Fig. 3. The cracked solid is subjected to an impact longitudinal wave (L-wave) loading described by

$$u_i^{\text{in}}(\mathbf{x}) = U_L D_i \cdot [c_L t - (x_1 + a)\sin\theta - x_2\cos\theta] \times H[c_L t - (x_1 + a)\sin\theta - x_2\cos\theta], \quad (55)$$

where $\mathbf{D} = (\sin\theta, \cos\theta)^T$ is the wave propagation vector for isotropic solids, U_L is the displacement amplitude of the incident L-wave, θ is the incidence angle, $H(\cdot)$ is the Heaviside function, and c_L is the longitudinal wave speed. The crack is divided into 41 elements of equal size. The time-step is taken as $c_T\,\Delta t = 0.05a$ with c_T being the transverse wave speed. Plane strain is assumed and Poisson's ratio is taken as 0.25. For a normal incidence of the L-wave with $\theta = 0°$, numerical results for the COD Δu_2 at several time instants are presented in Fig. 4 and compared to the numerical results obtained by the conventional time-domain BEM using the dynamic fundamental solution for isotropic solids [27]. Fig. 4 shows the time and the spatial variations of the COD Δu_2. The solid lines indicate the results obtained by the present time-domain traction BEM, while the dots are those provided by the conventional one. A good agreement between both numerical results is achieved.

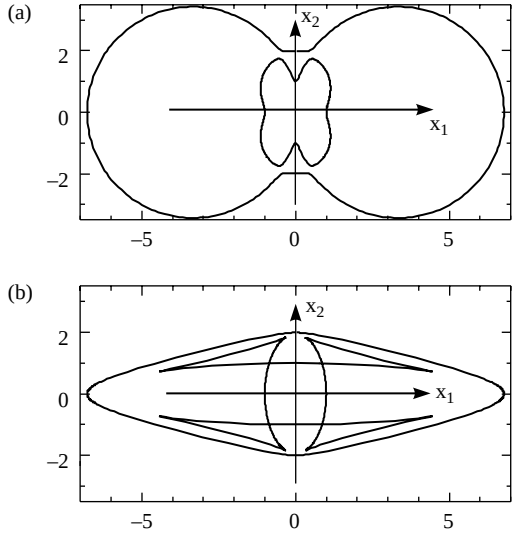

Fig. 5. (a) Plane wave velocity curves, and (b) wave front curves for a graphite–epoxy composite.

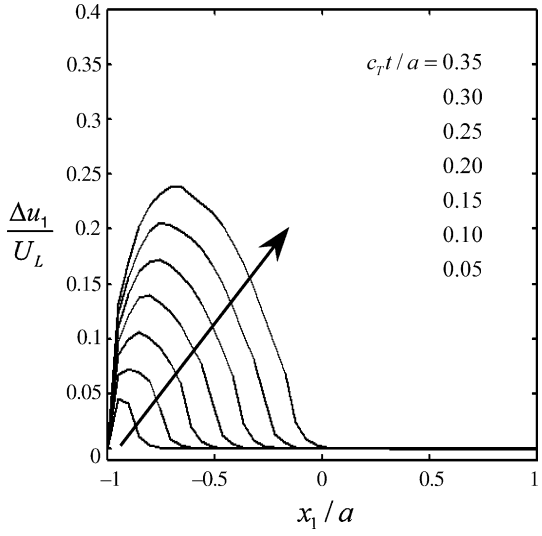

Fig. 7. Time variations of $\Delta u_1/U_L$ for a crack and a 45° incidence of a plane L-wave in an isotropic solid.

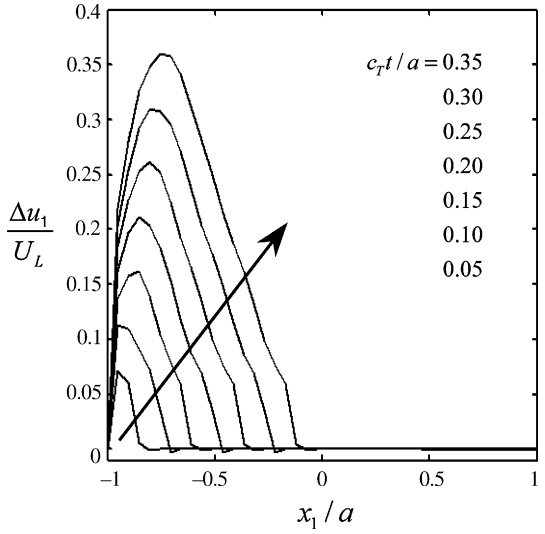

Fig. 8. Time variations of $\Delta u_2/U_L$ for a crack and a 45° incidence of a plane L-wave in an isotropic solid.

As next numerical example, we consider an infinite, transversely isotropic and linearly elastic solid with a finite crack of length $2a$ subjected to the same impact incident wave loading as described by Eq. (55), where c_L has now the meaning of the quasi-longitudinal wave speed. In this case, however, $\mathbf{D} \neq (\sin\theta, \cos\theta)^T$. The following elastic constants are used

$$C_{11} = C_{33} = 160.7 \text{ GPa}, \quad C_{12} = C_{23} = 6.44 \text{ GPa},$$

$$C_{22} = 13.92 \text{ GPa}, \quad C_{44} = C_{66} = 3.5 \text{ GPa},$$

$$C_{55} = (C_{33} - C_{13})/2 = 7.07 \text{ GPa}.$$

These elastic constants correspond to a graphite–epoxy composite [34]. The x_1-axis is taken as the axis of symmetry for the transversely isotropic solid.

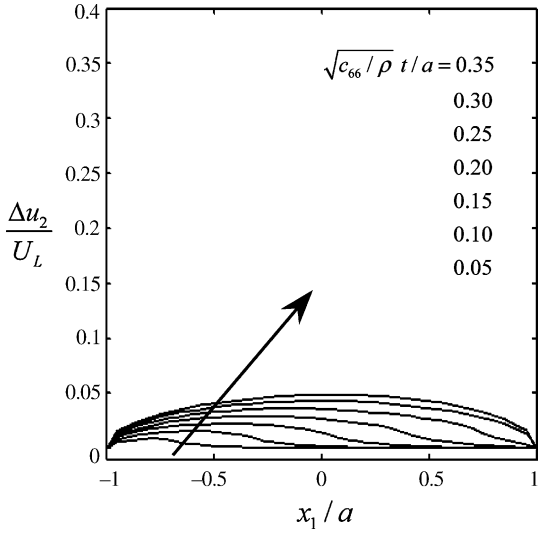

Fig. 9. Time variations of $\Delta u_1/U_L$ for a crack and a 45° incidence of a quasi L-wave in a transversely isotropic solid.

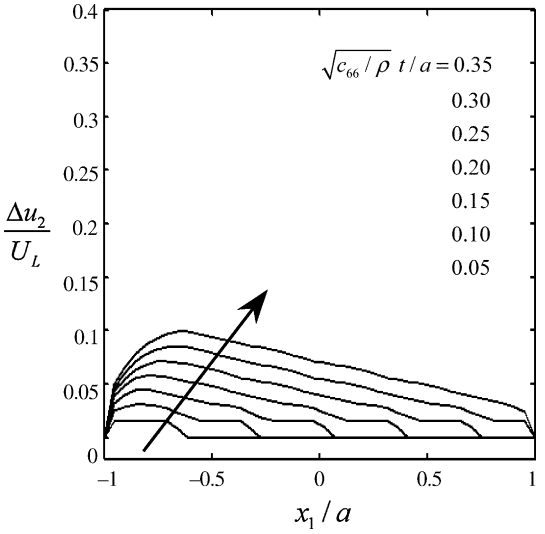

Fig. 10. Time variations of $\Delta u_2/U_L$ for a crack and a 45° incidence of a quasi L-wave in a transversely isotropic solid.

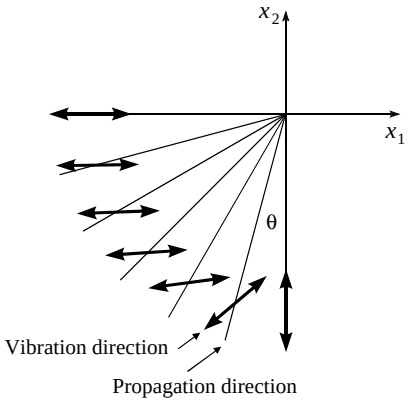

Fig. 11. Vibration directions of the incident wave with the corresponding propagation directions for graphite–epoxy composite.

Fig. 5 shows the plane wave velocity curves and the wavefront curves of the considered transversely isotropic solid. From Fig. 5a, it can be seen that the quasi-longitudinal wave speed is largest in the x_1-direction. The quasi-transverse wave speed increases first in directions away from the x_1-direction, but then shows a dip in

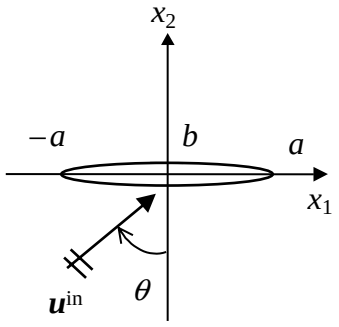

Fig. 12. An elliptical cavity.

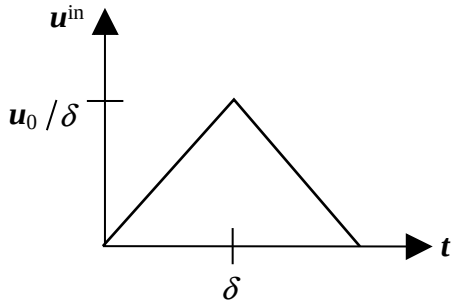

Fig. 13. Triangular pulse.

the x_2-direction. Since the velocity curves are concave in some ranges of the wave propagation directions, the wavefront curves may have peculiar shapes as shown in Fig. 5b. The wavefronts in the x_1-direction are quite simple: the longitudinal wave arrives first and the transverse wave follows. In contrast, the wavefronts near the x_2-direction are quite complicated: the significant differences there at neighboring points in the quasi-transverse wave speeds result in the overlapping wavefronts.

Fig. 6 shows the time variations of the normalized crack-opening-displacement $\Delta u_2/U_L$ for a crack subjected to a normal incidence of a quasi-longitudinal wave in a transversely isotropic solid. The results are quite similar to that of the isotropic one, with the exception of a slight difference in the curvature of the COD-curves near the crack-tips.

For an oblique incidence of a plane L-wave with $\theta = 45°$, numerical calculations have been carried out for both the isotropic and the transversely isotropic solids. Figs. 7 and 8 show the time variations of $\Delta u_1/U_L$ and $\Delta u_2/U_L$ for the isotropic solid, while Figs. 9 and 10 show the corresponding numerical results for the transversely isotropic solid. A comparison of the numerical results shows a quite different behavior in the time-variations of the CODs in isotropic and

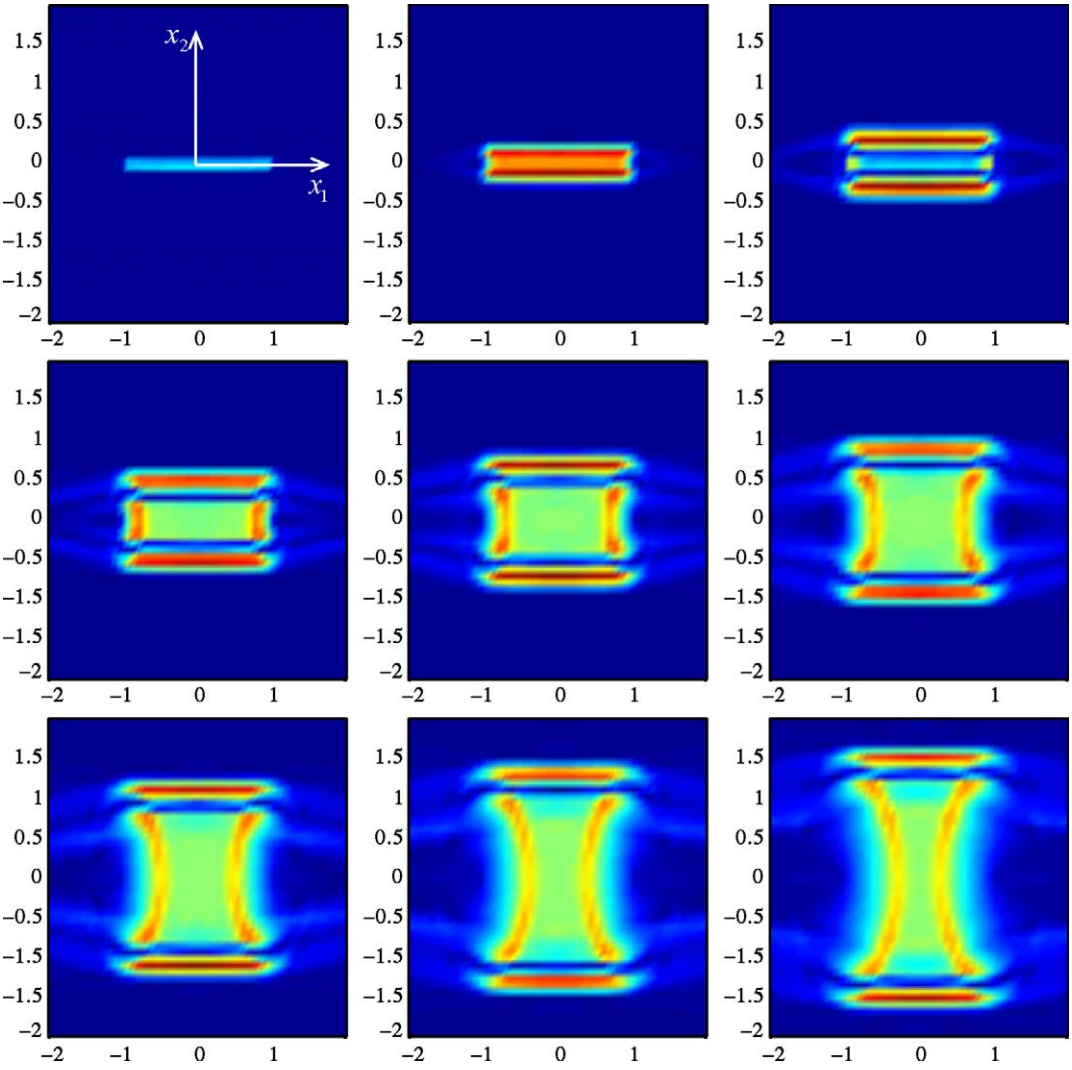

Fig. 14. Scattered wave field by an elliptical cavity for a normal incidence of a plane L-wave at times: $\sqrt{c_{66}/\rho}\, t/a = 0.05, 0.15, 0.25, 0.35, 0.45, 0.55, 0.65, 0.75,$ and 0.85.

transversely isotropic solids. At similar time-steps, the isotropic solid shows a larger value of the CODs in the range $x_1/a \in [-1, 0]$. This is because the vibration directions of the incident wave with the same propagation direction are different for both materials. Fig. 11 shows the vibration directions of the incident wave and the corresponding propagation directions for the considered transversely isotropic solid. Although the transversely isotropic solid has a smaller value of the CODs in the range $x_1/a \in [-1, 0]$, the CODs in the range of $x_1/a \in [0, 1]$ are not zero, in contrast to the isotropic case. The reason is that the wave velocity in the x_1-direction is much larger for the transversely isotropic solid than that for the isotropic one as can be seen in Fig. 5.

An additional reliability check to the present time-domain BEM has been made by considering an infinite, homogeneous, linearly elastic and transversely isotropic solid containing a very flat elliptical cavity subjected to an impact incident wave loading. To make the comparison possible, a flat elliptical cavity with a major axis of length $2a$ and an aspect ratio $b/a = 0.01$ as shown in Fig. 12 is investigated. The limit case $b/a \to 0$ corresponds to a crack of length $2a$. For the elliptical cavity, the boundary is divided into 80 elements and the time-domain displacement BEM of Wang et al. [48] has been applied, where a spatial collocation method was adopted. For the crack problem, 41 elements have been used. The same elastic constants as in the previous example have been chosen. An incident longitudinal or transverse wave with a triangular pulse shape as shown in Fig. 13 is considered, which is described by

$$u_i^{\text{in}}(\mathbf{x}) = \frac{u_0}{\delta} D_i \cdot [pH(p) - 2(p-\delta)H(p-\delta) - (p-2\delta)H(p-2\delta)], \tag{56}$$

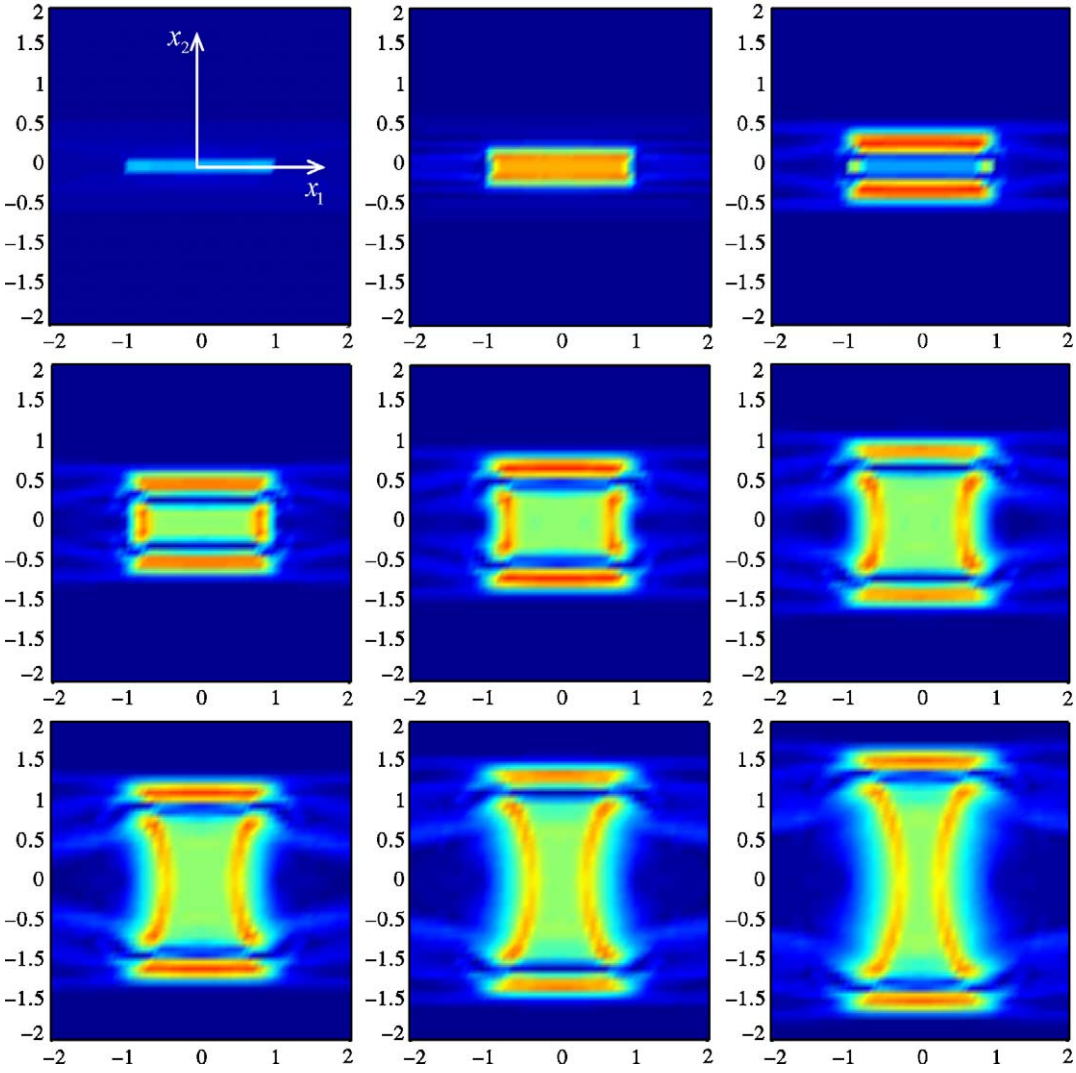

Fig. 15. Scattered wave field by a crack for a normal incidence of a plane L-wave at times: $\sqrt{c_{66}/\rho}\, t/a = 0.05, 0.15, 0.25, 0.35, 0.45, 0.55, 0.65, 0.75$, and 0.85.

where u_0 is the amplitude and 2δ is the base of the triangular pulse, and

$$p = t - \frac{x_2 + a}{c}, \quad \delta = \frac{0.25a}{c}, \tag{57}$$

with c being the velocity of the incident wave. Fig. 14 shows the images of the scattered displacement field by an elliptical cavity, while Fig. 15 presents the corresponding images due to a crack. The plotted values are the absolute values of the scattered displacements. Both figures show very similar results, which confirm the reliability of the present time-domain BEM for anisotropic solids. After the incident wave arrives at the crack, reflected waves by the crack-faces propagate in both forward and backward directions. Sideways wave scattering by the crack-tip can be seen clearly and is quite strong because of the higher wave speed in the x_1-direction. Sideways scattered waves propagate away from the crack-tips and the reflected waves move away from the crack. The quasi-transverse wave diffracted by the crack-tip can be identified at the normalized time 0.25. This pseudo-transverse wave produces an expanding wave-front moving away from the crack-tip. Due to the presence of the crack an intense deformation of the solid can be seen at the wave-front moving towards the center of the crack.

Finally, Fig. 16 shows the scattered displacement field due to a crack subjected to an oblique incidence of a plane transverse wave with an incidence angle $\theta = 45°$. Here again, the essential wave scattering characteristics in a cracked anisotropic solid can be identified.

It should be remarked here that the present time-domain BEM uses an explicit time-stepping scheme, which is only conditionally stable. The time-step has to be chosen properly to guarantee the stability and the quality of the method. According to our numerical experiences, the present method is stable if the time-step is selected in the range $0.5 \leq c\ \Delta t/L \leq 1.0$, where c is the smallest wave velocity and L is the element-length.

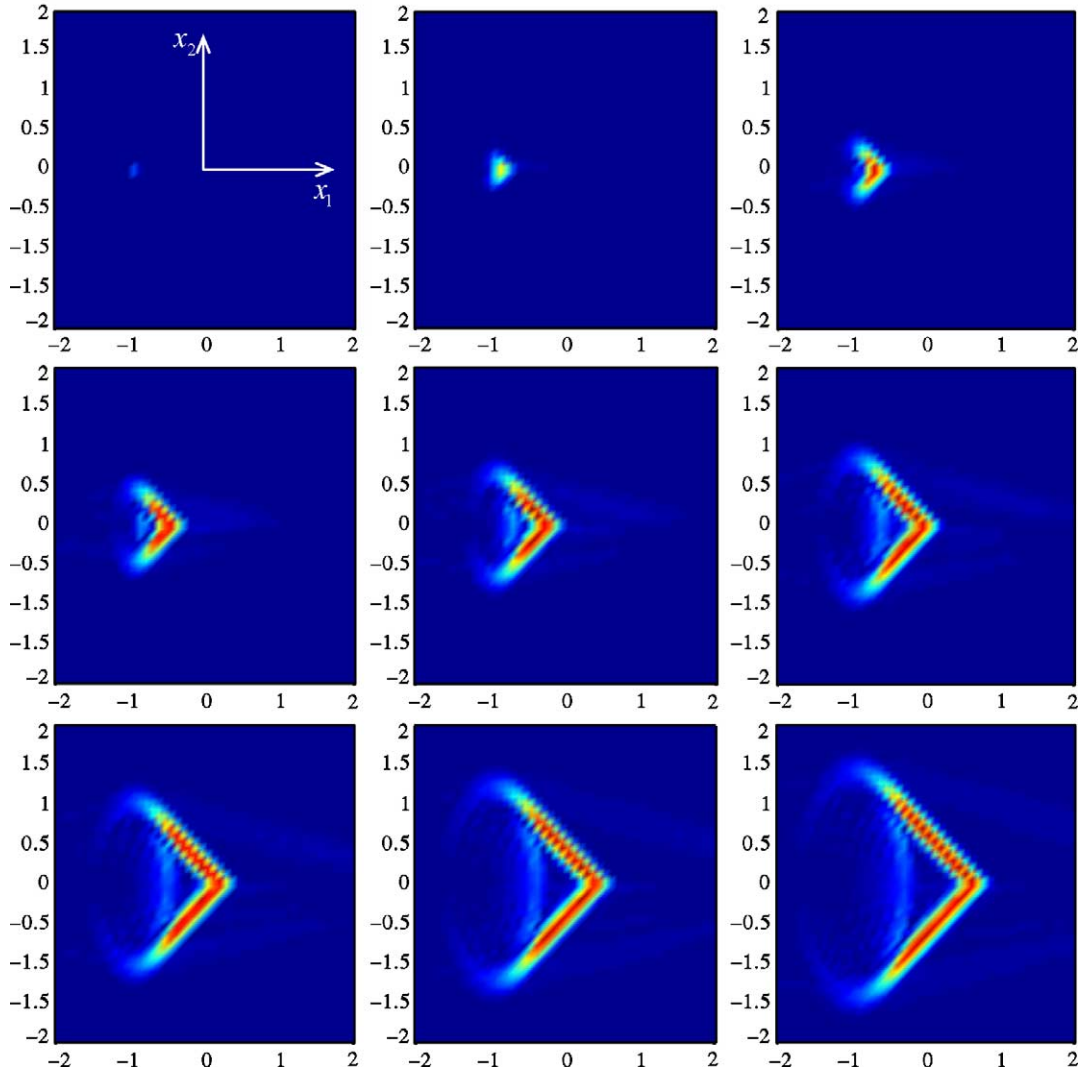

Fig. 16. Scattered wave field by a crack for a 45° oblique incidence of a plane transverse wave at times: $\sqrt{c_{66}/\rho}\ t/a = 0.05, 0.15, 0.25, 0.35, 0.45, 0.55, 0.65, 0.75,$ and 0.85.

7. Conclusions

A 2D time-domain traction BEM for transient wave scattering analysis by a crack in an anisotropic linearly elastic solid is presented in this paper. The method uses a collocation method for temporal discretization and a Galerkin-method for spatial discretization. By using linear temporal and spatial shape functions, the time convolution and the spatial integrations arising in the system matrices can be calculated analytically. The only integral to be computed numerically is the integral over the unit circle in the dynamic part of the fundamental solutions. The system matrices are symmetric and no special techniques are required in computing the hypersingular integrals. The accuracy and the reliability of the present time-domain BEM are verified by numerical examples for isotropic and transversely isotropic solids. An additional check has been made by comparing the numerical results for a crack with that obtained by a time-domain displacement BEM for a flat elliptical cavity in a transversely isotropic solid. Numerical examples show some very interesting features of scattered and reflected waves in a cracked anisotropic solid. The extension of the present method to finite, anisotropic and linearly elastic solids with cracks is in progress and the corresponding results will be reported in future.

Acknowledgements

The work of Ch. Zhang is supported by the German Research Foundation (DFG) under the project number ZH 15/5-1, which is gratefully acknowledged. A. Tan would also like to acknowledge the support from the University of the Philippines Diliman, where he is currently under study leave.

Appendix A. Analytical integration of the static system matrix

For an analytical integration of the static system matrix, it is convenient to introduce a local coordinate ζ for the element Γ_m and another local coordinate ξ for the element Γ_n, see Fig. A1. Then, Eq. (45) can be written as

$$W_{ij}^{s;m,n} = \frac{1}{\pi}\int_0^{h_m}\frac{\partial\phi_u^m(\zeta)}{\partial\zeta}\mathrm{d}\zeta\int_0^{n}\frac{\partial\phi_u^n(\xi)}{\partial\xi} \operatorname{Im}\sum_{l=1}^{L}\{B_{ij}^l(\eta_l)\log[\mathbf{d}_l\cdot(\mathbf{x}^{n-1}-\mathbf{y}^{m-1}) + \mathbf{d}_l\cdot\mathbf{s}^n\xi - \mathbf{d}_l\cdot\mathbf{s}^m\zeta]\}\mathrm{d}\xi, \tag{A.1}$$

where h_m and h_n denote the lengths of the mth element and the nth element, while $\mathbf{s}^m$ and $\mathbf{s}^n$ represent the unit vectors along the straight elements Γ_m and Γ_n (see Fig. A1). With

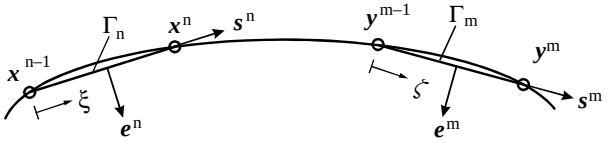

Fig. A1.. Discretization of the crack-face.

the following linear shape functions and their derivatives

$$\phi_u^n(\xi) = a\xi + b, \quad \frac{\partial\phi_u^n(\xi)}{\partial\xi} = a, \qquad \phi_u^m(\zeta) = c\zeta + d, \quad \frac{\partial\phi_u^m(\zeta)}{\partial\zeta} = c, \tag{A.2}$$

as well as the abbreviations

$$e = \mathbf{d}_l\cdot(\mathbf{x}^{n-1}-\mathbf{y}^{m-1}), \quad f = \mathbf{d}_l\cdot\mathbf{s}^n, \quad g = -\mathbf{d}_l\cdot\mathbf{s}^m, \tag{A.3}$$

we obtain the following analytical result for the integral in Eq. (A.1)

$$\begin{aligned}\int_0^{h_m} c\,\mathrm{d}\zeta\int_0^{h_n} a\log(e+f\xi+g\zeta)\mathrm{d}\xi &= \frac{ace^2\log(e)}{2fg} - \frac{ac(e+gh_m)^2\log(e+gh_m)}{2fg} \\ &\quad - \frac{ac(e+fh_n)^2\log(e+fh_n)}{2fg} \\ &\quad + \frac{ac(e+fh_n+gh_m)^2\log(e+fh_n+gh_m)}{2fg} \\ &\quad - \frac{3ach_mh_n}{2}.\end{aligned} \tag{A.4}$$

It should be noted here that e, f and g in Eq. (A.4) are complex constants. Since the complex log-function is multivalued, the branch-cuts of the log-function must be properly chosen.

Appendix B. Analytical integration of the dynamic system matrix

To perform the spatial integration of the dynamic system matrix analytically, we first substitute Eq. (50) into Eq. (46). Then, it is sufficient to consider the following integral

$$\int_{\Gamma_m}\phi_u^m(\mathbf{y})\mathrm{d}s_y\int_{\Gamma_n}\frac{1}{c_lq\,\Delta t+\mathbf{n}\cdot(\mathbf{x}-\mathbf{y})}\phi_u^n(x)\mathrm{d}s_x. \tag{B.1}$$

By using the local coordinates ζ and ξ, the linear shape functions (A.2) and the abbreviations

$$e = c_lq\,\Delta t+\mathbf{n}\cdot(\mathbf{x}^{n-1}-\mathbf{y}^{m-1}), \quad f = \mathbf{n}\cdot\mathbf{s}^n, \quad g = -\mathbf{n}\cdot\mathbf{s}^m, \tag{B.2}$$

we obtain from Eq. (B.1)

$$\int_0^{h_m}(c\zeta+d)\mathrm{d}\zeta\int_0^{h_n}(a\xi+b)\frac{1}{e+f\xi+g\zeta}\mathrm{d}\xi = A_1 e\log(e) - A_2(e+gh_m)\log(e+gh_m) + A_3(e+fh_n)\log(e+fh_n) - A_4(e+fh_n+gh_m) \times\log(e+fh_n+gh_m)+A_5, \quad (B.3)$$

where

$$A_1 = (-3bcef + ace^2 - 3adeg + 6bdfg)/(6f^2g^2), \quad (B.4)$$

$$A_2 = A_1 + (-2acg^2h_m - 3adg^2 + 3bcfg - aceg)h_m/(6f^2g^2), \quad (B.5)$$

$$A_3 = -A_1 + (2acf^2h_n + 3adfg + 3bcf^2 - acef)h_n/(6f^2g^2), \quad (B.6)$$

$$A_4 = -A_1 - [(2acg^2h_m + 3adg^2 + 3bcfg + aceg)h_m + 2acfgh_mh_n - (2acf^2h_n + 3bcf^2 - 3adfg + acef)h_n]/(6f^2g^2), \quad (B.7)$$

$$A_5 = (3adg + 2acgh_m + 2acfh_n + 3bcf + ace)h_mh_n/(6fg). \quad (B.8)$$

References

[1] Achenbach JD. Wave propagation in elastic solids. Amsterdam: North-Holland; 1973.

[2] Albuquerque EL, Sollero P, Aliabadi MH. The boundary element method applied to time dependent problems. Int J Solids Struct 2002; 39:1405–22.

[3] Albuquerque EL, Sollero P, Fedelinsky P. Dual reciprocity boundary element method in Laplace-domain applied to anisotropic dynamic crack problems. Computers Struct 2003;81:1703–13.

[4] Albuquerque EL, Sollero P, Aliabadi MH. Dual boundary element method for anisotropic dynamic fracture mechanics. Int J Numer Meth Eng 2004;59:1187–205.

[5] Aliabadi MH, Rooke DP. Numerical fracture mechanics. Southampton, UK: Computational Mechanics Publications; 1991.

[6] Aliabadi MH. Boundary element formulations in fracture mechanics. Appl Mech Rev 1997;50:83–96.

[7] Ariza MP, Dominguez J. Dynamic BE analysis of 3-D cracks in transversely isotropic solids. Comput Meth Appl Mech Eng 2004;193: 765–79.

[8] Balas J, Sladek J, Sladek V. Stress analysis by boundary element methods. Amsterdam: Elsevier; 1989.

[9] Beskos DE. Boundary element methods in dynamic analysis: part II (1986–1996). Appl Mech Rev 1997;50:149–97.

[10] Bonnet M. Boundary integral equation methods for solids and fluids. New York: Wiley; 1999.

[11] Boström A, Grahn T, Niklasson AJ. Scattering of elastic waves by a rectangular crack in an anisotropic solid—modelling of ultrasonic nondestructive testing. Research report 2. Göteborg, Sweden: Department of Applied Mechanics, Chalmers University of Technology; 2002.

[12] Boström A, Grahn T, Niklasson AJ. Scattering of elastic waves by a rectangular crack in a thick-walled anisotropic solid—modelling of ultrasonic nondestructive testing. Research report 3. Göteborg, Sweden: Department of Applied Mechanics, Chalmers University of Technology; 2002.

[13] Boström A, Grahn T, Niklasson AJ. Scattering of elastic waves by a rectangular crack in an anisotropic half-space. Wave Motion 2003;38: 91–107.

[14] Boström A. Review of hypersingular integral equation method for crack scattering and application to modeling of ultrasonic nondestructive evaluation. Appl Mech Rev 2003;56:383–405.

[15] Chen JT, Hong H-K. Review of dual boundary element methods with emphasis on hypersingular integrals and divergent series. Appl Mech Rev 1999;52:17–33.

[16] Cruse TA. Boundary element analysis in computational fracture mechanics. Boston: Kluwer; 1988.

[17] Denda M. A dislocation and a point force approach to the boundary element method for mixed crack analysis of plane anisotropic solids. J Chin Inst Eng 1999;22:1–17.

[18] Denda M. Mixed mode I, II, and III analysis of multiple cracks in plane anisotropic solids by the BEM: a dislocation and point force approach. Eng Anal Bound Elem 2001;25:267–78.

[19] Denda M, Wang CY, Yong YC. 2D time-harmonic BEM for solids of general anisotropy with application to eigenvalue problems. J Sound Vib 2003;261:247–76.

[20] Denda M, Mattingly E. The whole crack singular element for 2-D boundary element analysis of multiple straight cracks in the general anisotropic solids. Electr J Bound Elem 2003;1:404–17.

[21] Denda M, Marante ME. Mixed mode BEM analysis of multiple curvilinear cracks in the general anisotropic solids by the crack tip singular element. Int J Solids Struct 2004;41:1473–89.

[22] Domínguez J. Boundary elements in dynamics. Southampton, UK: Computaional Mechanics Publications; 1993.

[23] Fedelinski P, Aliabadi MH, Rooke DP. A single-region time-domain BEM for dynamic crack problems. Int J Solids Struct 1995;32: 3555–71.

[24] Fedelinski P. Boundary element method in dynamic analysis of structures with cracks. Eng Anal Bound Elem 2004;28:1135–47.

[25] Garcia F, Saez A, Dominguez J. Traction boundary elements for cracks in anisotropic solids. Eng Anal Bound Elem 2004;28:667–76.

[26] Garcia F, Saez A, Dominguez J. Anisotropic and piezoelectric materials fracture analysis by BEM. Computers Struct; 2005;83:804–820.

[27] Hirose S, Achenbach JD. Time-domain boundary element analysis of elastic wave interaction with a crack. Int J Numer Meth Eng 1989;28: 629–44.

[28] Hirose S. Dynamic analysis for a crack in anisotropic elastic solid (in Japanese). JASCOME 1999;16:13–17.

[29] Hirose S, Wang C-Y, Achenbach JD. Boundary element method for elastic wave scattering by a crack in an anisotropic solid. 20th international congress for theoretical and applied mechanics, ICTAM 2000, Chicago, USA, 27 August–2 September 2000.

[30] Hirose S, Zhang Ch, Wang C-Y. A comparative study on two time-domain BEM/BIEM for transient dynamic crack analysis of anisotropic solids. In: Yao Zhenhan, Aliabadi MH, editors. Boundary element techniques. New York: Tsinghua University Press/Springer; 2002. p. 106–12.

[31] Hong H-K, Chen JT. Derivation of integral equations of elasticity. ASCE J Eng Mech 1988;114:1028–44.

[32] Izumi A, Hirose S. Crack growth analysis in anisotropic solids. Technical report no. 62. Tokyo, Japan: Department of Civil Engineering. Tokyo Institute of Technology; 2000 p. 3–15.

[33] Manolis GD, Beskos DE. Boundary element methods in elastodynamics. London, UK: Unwin Hyman Ltd; 1988.

[34] Musgrave MJP. Crystal acoustics. San Francisco, USA: Holden-Day, Inc; 1970.

[35] Nishimura N, Kobayashi S, Kishima T. A BIE analysis of wave propagation in anisotropic media. In: Tanaka M, Brebbia CA, editors. Boundary elements VIII. New York: Springer; 1986. p. 425–34.
[36] Pan E. A general boundary element analysis of 2-D linear elastic fracture mechanics. Int J Fract 1997;88:41–59.
[37] Pan E, Yuan FG. Boundary element analysis of three-dimensional cracks in anisotropic solids. Int J Numer Meth Eng 2000;48:211–37.
[38] Portela A, Aliabadi MH, Rooke DP. The dual boundary element method: effective implementation for crack problems. Int J Numer Meth Eng 1992;33:1269–87.
[39] Saez A, Dominguez J. BEM analysis of wave scattering in transversely isotropic solids. Int J Numer Meth Eng 1999;44: 1283–300.
[40] Saez A, Dominguez J. Dynamic crack problems in three-dimensional transversely isotropic solids. Eng Anal Bound Elem 2001;25:203–10.
[41] Sladek V, Sladek J. Regularization of hypersingular integrals in BEM formulations using various kinds of continuous elements. Eng Anal Bound Elem 1996;17:5–18.
[42] Snyder MD, Cruse TA. Boundary integral equation analysis of cracked anisotropic plates. Int J Fract 1975;11:315–28.
[43] Sollero P, Aliabadi MH. Anisotropic analysis of cracks in composite laminates using dual boundary element method. Compos Struct 1995; 31:229–33.
[44] Stroh AN. Dislocations and cracks in anisotropic elasticity. Phil Mag 1958;7:625–46.
[45] Tanaka M, Sladek V, Sladek J. Regularization techniques applied to boundary element methods. Appl Mech Rev 1994;47:457–99.
[46] Ting TCT. Anisotropic elasticity. Oxford: Oxford University Press; 1996.
[47] Wang C-Y, Achenbach JD. Elastodynamic fundamental solutions for anisotropic solids. Geophys J Int 1994;118:384–92.
[48] Wang C-Y, Achenbach JD, Hirose S. Two-dimensional time domain BEM for scattering of elastic waves in solids of general anisotropy. Int J Solids Struct 1996;33:3843–64.
[49] Wang C-Y. Elastic fields produced by a point source in solid of general anisotropy. J Eng Math 1997;32:41–52.
[50] Zhang Ch, Gross D. On wave propagation in elastic solids with cracks. Southampton, UK: Computational Mechanics Publications; 1998.
[51] Zhang Ch, Savaidis A. Time-domain BEM for dynamic crack analysis. Math Comput Simul 1999;50:351–62.
[52] Zhang Ch. Transient elastodynamic antiplane crack analysis of anisotropic solids. Int J Solids Struct 2000;37:6107–30.
[53] Zhang Ch, Savaidis A, Savaidis G. Dynamic crack analysis of anistropic solids under impact loading. In: Matzen VC, David Tung CC, editors. Transactions of the 16th international confernce on structural mechanics in reactor technology. Paper No. 1981. USA: Center for Nuclear Power Plant Structures, Equipment and Piping, North Carolina State University; 1981.
[54] Zhang Ch. A 2-D time-domain BIEM for dynamic analysis of cracked orthotropic solids. Computer Model Eng Sci 2002;3:381–98.
[55] Zhang Ch. A 2-D hypersingular time-domain traction BEM for transient elastodynamic crack analysis. Wave Motion 2002;35: 17–40.